JACS Au
AN OPEN ACCESS JOURNAL OF THE AMERICAN CHEMICAL SOCIETY

pubs.acs.org/jacsau
Article

Understanding the Pathway Switch of the Oxygen Reduction Reaction from Single- to Double-/Triple-Atom Catalysts: A Dual Channel for Electron Acceptance−Backdonation

Jin Liu,[§] Haoxiang Xu,[§] Jiqin Zhu, and Daojian Cheng*

Cite This: JACS Au 2023, 3, 3031−3044
Read Online

ACCESS | Metrics & More | Article Recommendations | Supporting Information

ABSTRACT: Recently, a lot of attention has been dedicated to double- or triple-atom catalysts (DACs/TACs) as promising alternatives to platinum-based catalysts for the oxygen reduction reaction (ORR) in fuel cell applications. However, the ORR activity of DACs/TACs is usually theoretically understood or predicted using the single-site association pathway ($O_2 \rightarrow OOH^* \rightarrow O^* \rightarrow OH^* \rightarrow H_2O$) proposed from Pt-based alloy and single-atom catalysts (SACs). Here, we investigate the ORR process on a series of graphene-supported Fe−Co DACs/TACs by means of first-principles calculation and an electrode microkinetic model. We propose that a dual channel for electron acceptance−backdonation on adjacent metal sites of DACs/TACs efficiently promotes O−O bond breakage compared with SACs, which makes ORR switch to proceed through dual-site dissociation pathways ($O_2 \rightarrow O^* + OH^* \rightarrow 2OH^* \rightarrow OH^* \rightarrow H_2O$) from the traditional single-site association pathway. Following this revised ORR network, a complete reaction phase diagram of DACs/TACs is established, where the preferential ORR pathways and activity can be described by a three-dimensional volcano plot spanned by the adsorption free energies of $\Delta G(O^*)$ and $\Delta G(OH^*)$. Besides, the kinetics preferability of dual-site dissociation pathways is also appropriate for other graphene- or oxide-supported DACs/TACs. The contribution of dual-site dissociation pathways, rather than the traditional single-site association pathway, makes the theoretical ORR activity of DACs/TACs in better agreement with available experiments, rationalizing the superior kinetic behavior of DACs/TACs to that of SACs. This work reveals the origin of ORR pathway switching from SACs to DACs/TACs, which broadens the ideas and lays the theoretical foundation for the rational design of DACs/TACs and may also be heuristic for other reactions catalyzed by DACs/TACs.

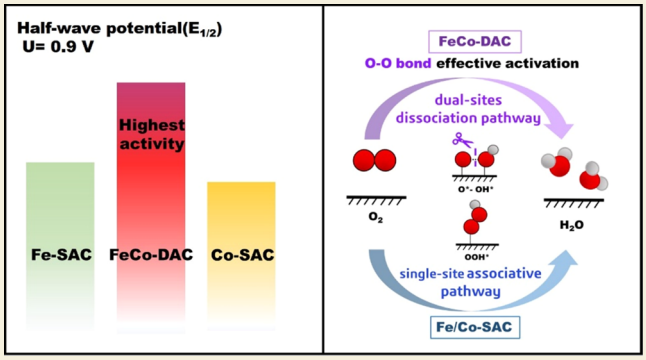

KEYWORDS: *double-atom catalysts (DACs), triple-atom catalysts (TACs), ORR pathway, dual-site dissociation pathway, DFT calculation*

1. INTRODUCTION

Atomically dispersed metal catalysts (ADMCs) with well-defined structures, especially for single-atom catalysts (SACs) and multi-atom catalysts (such as double-atom catalysts (DACs), triple-atom catalysts (TACs)), have attracted great interest in heterogeneous catalysis in recent years.[1,2] SACs exhibit distinct catalytic properties compared to metal nanoparticles (NPs) due to their uniform active sites and high metal utilization.[3−5] However, SACs only provide an isolated adsorption site for catalytic reactions. For catalytic reactions involving the adsorption and coupling of multiple molecules, such as the hydrocarbon hydrogenation reaction and CO_2 reduction reaction (CO_2RR), it is rather challenging to improve the catalytic performance of SACs.[6] Compared with SACs, the multiple active sites of DACs/TACs may render them versatile binding modes toward adsorbates due to their diverse synergistic interactions, thus improving their ability to surpass the intrinsic performance by circumventing the scaling relationship.[7,8] Nowadays, DACs/TACs have attracted considerable research interest, since they exhibit remarkable catalytic performances in a variety of reactions, including thermocatalysis,[9−11] photocatalysis,[12] and electrocatalysis.[13−15]

The electrochemical oxygen reduction reaction (ORR) has gained widespread attention by virtue of its significance in energy storage and conversion, including metal−air batteries and proton-conducting membrane fuel cells.[2,16] Platinum-based nanomaterials have been investigated experimentally and computationally in depth over the past decade because they

Received: August 2, 2023
Revised: August 23, 2023
Accepted: August 28, 2023
Published: October 21, 2023

are effective and durable ORR catalysts,[17−21] but they are too expensive for large-scale applications. Nonprecious-metal carbon-based atomically dispersed catalysts with metal−nitrogen coordination sites, especially for Fe-involved or Co-involved composites,[22−24] have attracted broad research interest in recent years because of their relatively high ORR activity and low cost.[25,26] Many experimental tests and theoretical studies have been devoted to elucidating the electrocatalytic mechanism of ORR. The current understanding of the superior ORR performance of DACs/TACs to SACs is still based on the single-site associative mechanism ($O_2 \rightarrow OOH^* \rightarrow O^* \rightarrow OH^* \rightarrow H_2O$). Only one of the metal sites (M_1) in DACs/TACs serves as an active center, while the others are spectators modifying the electronic configuration of M_1, thus enhancing the intrinsic activity of the M_1 site.[23,27] Besides, theoretical or high-throughput screening for DACs/TACs aided by density functional theory (DFT) calculation is similar to that for Pt-based nanomaterials, which is still based on the associative mechanism[28] and the activity volcano trend spanned by adsorption free energies of OH*.[29−33] However, in contrast to metal particles with continuous zero valence metal sites, the contiguous metal cations of DACs/TACs provide a desired synergistic effect altering intrinsic catalytic ability, which in turn renders the possibility to tune a reaction pathway. Compared with SACs, DACs/TACs possess multiple active sites to bind with the adsorbent with different modes, so that the reaction can proceed through another pathway with kinetics preferability.[34−37] In recent experimental work, Wang et al.[38] and Liu et al.[39] adjusted the atomic distance of single-atom pairs to induce O−O radical breakage without forming redundant *OOH intermediates, which causes the ORR to follow the dissociated ORR pathway. Therefore, it is reasonable to infer that unique charge distribution at the active site of DACs/TACs may contribute to promoting the delocalized electron transfer between the orbital of O_2 and DACs/TACs, and accordingly, ORR may possess new reaction pathways[40] on DACs/TACs, which accounts for their superior activity to SACs.[41−43]

Herein, we identify a dual channel for electron acceptance−backdonation between adjacent metal sites of DACs/TACs and the O−O bond, leading to greater activation and easier cleavage of the O−O bond on DAC/TACs than those on SACs. A total of 15 Fe−Co DACs and 20 Fe−Co TACs supported on graphene are established to evaluate the ORR process, demonstrating the universality of preferential pathway switching from the single-site association pathway to the dual-site dissociation pathway, due to O−O bond activation by the dual channel for electron acceptance−backdonation. Following this revised ORR network, a complete reaction phase diagram of DACs/TACs is established. It shows that the reaction pathways, potential determining step, and activity of ORR over DACs/TACs can be described by a three-dimensional volcano plot spanned by the adsorption free energies of $\Delta G(O^*)$ and $\Delta G(OH^*)$. Finally, the domination of the dual-site dissociation pathway on ORR can be extended to other carbon- or oxide-supported DACs/TACs. Hence, this work has a deep understanding and rationalizes the superior ORR kinetic behavior of DACs/TACs to SACs in available experiments, which opens up a new way for the rational design of DACs/TACs.

2. COMPUTATIONAL METHODS

All of the computations were carried out by the spin-polarized DFT method, as implemented in the Vienna Ab initio Simulation Package (VASP) 5.4 code.[44,45] The exchange−correlation energy was modeled by the Perdew−Burke−Ernzerhof (PBE) functional.[46,47] Among the extensively theoretical computational works, a N-doped graphene monolayer has been regarded as an efficient theoretical model to represent the carbon-based support of ADMCs.[38,48−50] In this work, graphene was modeled with a (5×5) supercell, and a vacuum slab of 15 Å was inserted in the z direction for surface isolation to prevent the interaction between two neighboring surfaces. The DFT + U method with $U - J = 3.0$ eV was used to describe the strong correlation of the localized Fe/Co 3d states.[51] The magnetic moment of Fe/Co was calculated, allowing the magnitude to change during the optimization. An energy cutoff of 500 eV was adopted for the plane-wave basis. In structural optimizations, the Brillouin zone was sampled by $3 \times 3 \times 1$ k-points using the Monkhorst−Pack scheme, while denser k-points of $6 \times 6 \times 1$ were employed for electronic property computations. The energy and force convergence criteria are 10^{-5} eV and 0.02 eV/Å, respectively. The adsorption free energy of each adsorbate is defined as follows

$$\Delta G = \Delta E - T\Delta S + \Delta E_{ZPE} + \Delta E_{solv} \quad (1)$$

where ΔE is the energy change from DFT calculations, ΔE_{ZPE} is the zero-point energy change, and ΔS is the entropy change at 298.15 K. The adsorption free energy ΔG_{OOH^*}, ΔG_{O^*}, and ΔG_{OH^*} are relative to the free energy of stoichiometrically appropriate amounts of H_2O (l) and H_2 (g). The solvent effect (ΔE_{solv}) was tested by using an implicit solvation model of the VASPsol code.[52,53] At the common ORR temperature of 298.15 K, the dielectric constant of water is 78.36 F/m. Referring to relevant calculation references,[53,54] the dielectric constant of 80 was approximately set to simulate the aqueous electrolyte. The effective surface tension parameter was assigned to 0 in VASPsol to neglect the cavitation energy contribution. The Debye length is set to 3.0 Å. ΔE_{solv} refers to the stabilization of the adsorbate because of the interaction with surrounding water.

Activation barriers for all proton−electron transfer steps of intermediates were set at 0.26 eV taken from Pt(111),[18] which has been successfully applied in ADMCs.[33,55] We calculated the activation barriers of the reaction involved with O−O bond breaking, using the climbing image nudged elastic band (CINEB)[56] method.

The reaction free energies at constant potential were determined by combining the capacitor model developed by Chan and Nørskov[57,58] and the computational hydrogen electrode (CHE) model proposed by Nørskov et al.[59] We first used the capacitor model[57,58] to convert the constant-charge simulations to the actual electrochemical constant-potential conditions. The charge transfer (the Bader charge of the surface) and work function of state 1(Φ_1) and state 2 (Φ_2) were calculated based on the optimized structures from density functional theory (DFT) calculations. All of the calculated charge transfers were referenced to state 2 in each of the elementary steps, and a change of work function was used to build the linear relations. The free energy changes between the two states (i.e., state 1 and state 2) at constant work functions thus are given by

$$G_2(\Phi_1) - G_1(\Phi_1) = G_2(\Phi_2) - G_1(\Phi_1) + (q_2 - q_1)(\Phi_2 - \Phi_1)/2 \quad (2)$$

$$G_2(\Phi_2) - G_1(\Phi_2) = G_2(\Phi_2) - G_1(\Phi_1) + (q_2 - q_1)(\Phi_2 - \Phi_1)/2 \quad (3)$$

in which $G_1(\Phi_1)$ and $G_2(\Phi_2)$ represent the DFT-calculated free energies of the optimized initial and final states, respectively, Φ_1 and Φ_2 are the work functions of the optimized initial state and final state relative to the vacuum energy level, and q_1 and q_2 are the excess surface charges, at states 1 and 2 simulated with constant charge, respectively. $\Phi(U = 0\ V)$ is the value of Φ at which the horizontal line $\Delta G = \Delta G_{CHE}(U = 0\ V)$ and line $\Delta G = \Delta G(\Phi)$ intersect.

https://doi.org/10.1021/jacsau.3c00432
JACS Au 2023, 3, 3031−3044

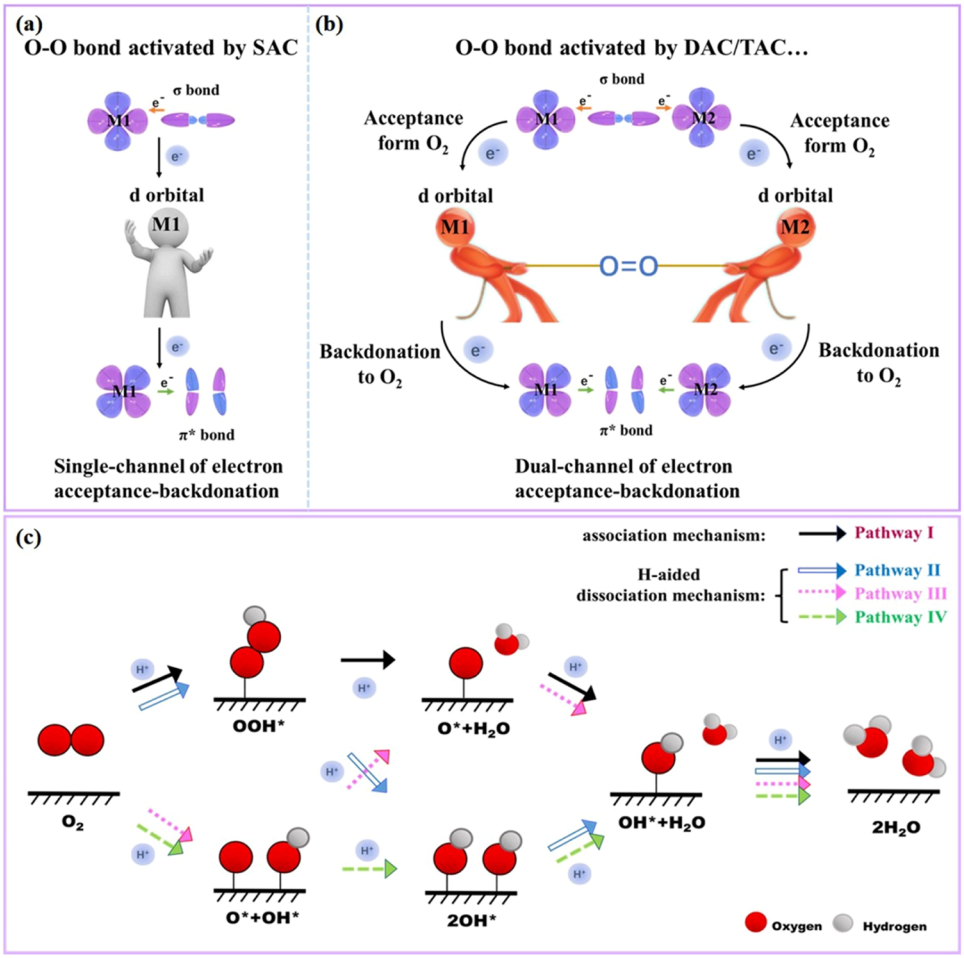

Figure 1. (a) Schematic diagram of the single channel of electron acceptance−backdonation for the O−O bond activated by SACs. (b) Schematic diagram of the dual channel of electron acceptance−backdonation for the O−O bond activated by DACs/TACs. (c) Schematic depiction of the single-site associative pathway and dual-site dissociation pathways for O_2 electrochemical reduction.

3. RESULTS AND DISCUSSION

3.1. Dual Channel for Electron Acceptance−Backdonation on Adjacent Metal Sites to Activate the O−O Bond

Generally, the widely accepted ORR pathway is a single-site associative mechanism ($O_2 \rightarrow OOH^* \rightarrow O^* \rightarrow OH^* \rightarrow H_2O$), which was originally developed from extended metal surfaces and is now also commonly employed in ADMCs. However, the mechanism of O_2 reduction can be very different on DACs/TACs compared with extended metal surfaces or SACs. Active centers in DACs/TACs not only optimize the electronic structure of adjacent metal centers through the short/medium-range electron interaction but also provide an additional adsorption site to change the intermediate adsorption. Previous reports have noted the probable existence of side-on adsorption of O_2* or OOH*, where each adjacent active site binds to an O atom to form dual-side adsorption on DACs/TACs,[60] offering the opportunity to further accelerate multi-intermediate conversion reactions.[61,62]

The "acceptance−backdonation" mechanism, usually used to explain the adsorption and activation process of small molecules (N_2*, CO*, etc.) on transition metal catalysts,[63−65] was introduced to understand the activation mechanism of O_2 molecules on ADMCs. When adsorbates containing O−O bonds are adsorbed on SACs (Figure 1a), the lone-pair electrons from the σ orbital of the O−O bond transfer to empty d-orbitals of isolated metal atoms, and simultaneously, the partially filled d-electrons of isolated metal atoms transfer electrons to π^* orbitals of the O−O bond, thus activating the O−O bond. However, electrons only transfer from one side of the O−O bond upon adsorption on solo metal centers of SACs, namely, a single channel of electron acceptance−backdonation. As shown in Figure 1b, the adjacent metal sites of DACs/TACs could provide an additional adsorption site to form a side-on O_2 adsorption mode, so we suggest a "dual channel of electron acceptance−backdonation" mechanism to understand the activation mechanism of the O−O bond on DACs. The lone-pair electrons from the σ orbital of O_2 may transfer from both sides of the O−O bond (or dual channels) to empty the d orbital of the adjacent metal sites, and the d-electrons of the metal sites may also donate back part of the electrons to O_2 through dual channels. Compared with SACs, the dual channel of electron acceptance−backdonation of DACs/TACs enables more efficient orbital overlap between metal and O atoms, leading to better activation of the O−O bond. When the active centers of DACs/TACs are involved in the interaction with the O−O bond, both M_1−O and M_2−O bonds have strong binding abilities, so that both M_1 and M_2 have a large pulling force on the O−O bond, which is conducive to the dissociation of the O−O bond. Due to the "dual channel of electron acceptance−backdonation" mechanism-induced O−O bond activation, dissociation pathways involving O−O breakage during ORR

https://doi.org/10.1021/jacsau.3c00432
JACS Au 2023, 3, 3031−3044

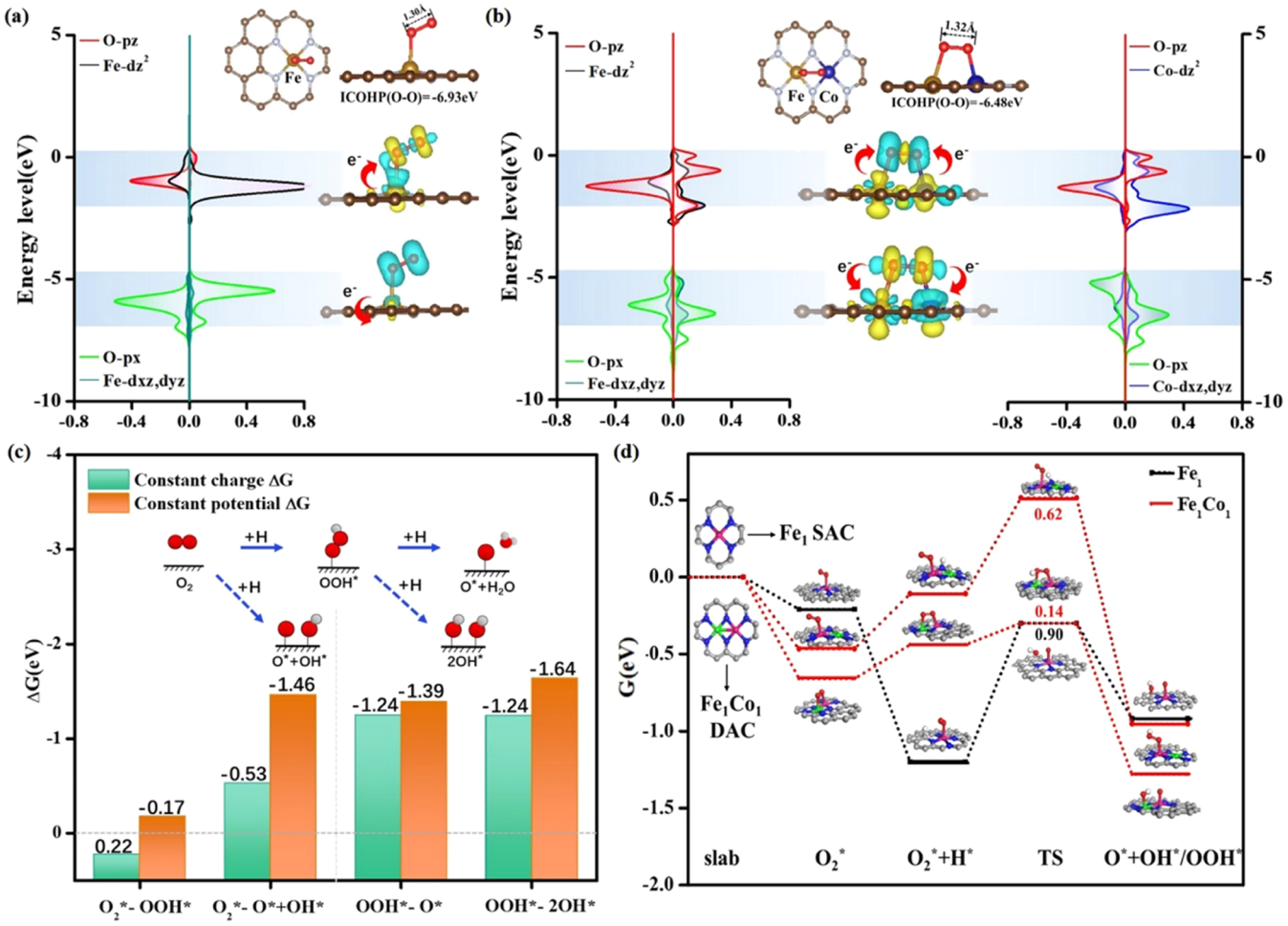

Figure 2. Partial differential charge density projecting to the specific energy level. The projected density of state between the O_2 molecule on (a) Fe-SAC and (b) Fe_1Co_1-DAC. (The blue area represents the loss of electrons, and the yellow area represents the gain of electrons. The Fermi energy is set to 0 eV.) (c) The reaction free energy (at 0.9 V vs RHE) of the competing steps between single-site association and dual-site dissociation mechanisms on Fe_1Co_1-DAC, according to the constant-charge and constant-potential method. (d) The O−O bond cleavage barrier of O_2* along with hydrogenation on Fe-SAC and Fe_1Co_1-DAC. The associative pathway barrier of O_2* + H → OOH* on Fe_1Co_1-DAC. The free energies of Fe-SAC and Fe_1Co_1-DAC with no adsorption are set as references for other intermediates along the reaction (G = 0 eV).

on DACs/TACs should not be overlooked. Here, we further supplement possible ORR routes for DACs/TACs, as shown in Figure 1c, where O_2 and OOH intermediates proceed to dissociation on DACs/TACs and generate stable 2OH* and O* + OH* intermediates. The complete reaction pathway with all possible intermediates and electrochemical steps is constructed, where pathway I is a traditional single-site associative pathway and pathways II−IV are dual-site dissociation pathways.

There are many experimental reports on N-doped graphene as the supporting material for dual metal sites.[66−68] Besides, FeCo DACs have been reported more than once to possess superior ORR activity to Fe SACs or Co SACs in the experiment.[23,32,69] Therefore, $Fe_1Co_1-N_6$ and Fe_1-N_4 embedded in graphene were chosen as prototypes (Figure 2a), and the "dual channel of electron acceptance−backdonation" mechanism was applied to rationalize the more activation of the O−O bond and higher ORR activity on Fe_1Co_1-DAC than those on Fe-SAC. Adsorption of a single O_2 molecule on Fe_1Co_1-DAC occurs via a side-on configuration with the formation of Fe−O and Co−O bonds (Figure S1). It is actually more favorable by 0.09 eV than that of the endon configuration. Figures 2a,b and S2a show the activation mechanism of O_2* adsorbed on Fe-SAC and Fe_1Co_1-DAC according to the projected density of state and partial differential charge density projecting to the specific energy level.[70,71] When O_2* is adsorbed on Fe-SAC, the electrons of the σ orbital of the O−O bond contributed by O $2p_x$ orbital transfer to d_{xz} and d_{yz} orbitals of Fe in the energy level from −5 to −7 eV. At the same time, the electrons from the partially filled Fe d_{z^2} orbital flow back into the π^* orbitals of the O−O bond in the energy level of 0−−2 eV. Fe_1Co_1-DAC provides an additional adsorption site to form bonds with both ends of O_2, forming a dual channel of electron acceptance−backdonation in the corresponding energy level, which could be conducive to the sufficient activation of O_2. The O−O bond length is elongated to 1.33 Å on Fe_1Co_1-DAC, which is longer than that on Fe-SAC (1.30 Å). The O−O bond strength on Fe_1Co_1-DAC (ICOHP = −6.48 eV) is weaker than that on Fe_1-SAC (ICOHP = −6.93 eV). These could be ascribed to the strong hybridization between Fe $3d_{z^2}$, Co $3d_{z^2}$, and O $2p_z$ orbitals in O_2@Fe_1Co_1-DAC, which increases delocalized electron transfer between O_2 and FeCo sites and promotes dissociation of O_2 for ORR. The dual channel of electron acceptance−backdonation is still observed between the O−O bond of OOH* on Fe_1Co_1-DAC (Figure S2).

To evaluate the thermodynamic and kinetic priority of O−O bond dissociation on DACs/TACs, the reaction free energy of

https://doi.org/10.1021/jacsau.3c00432
JACS Au 2023, 3, 3031−3044

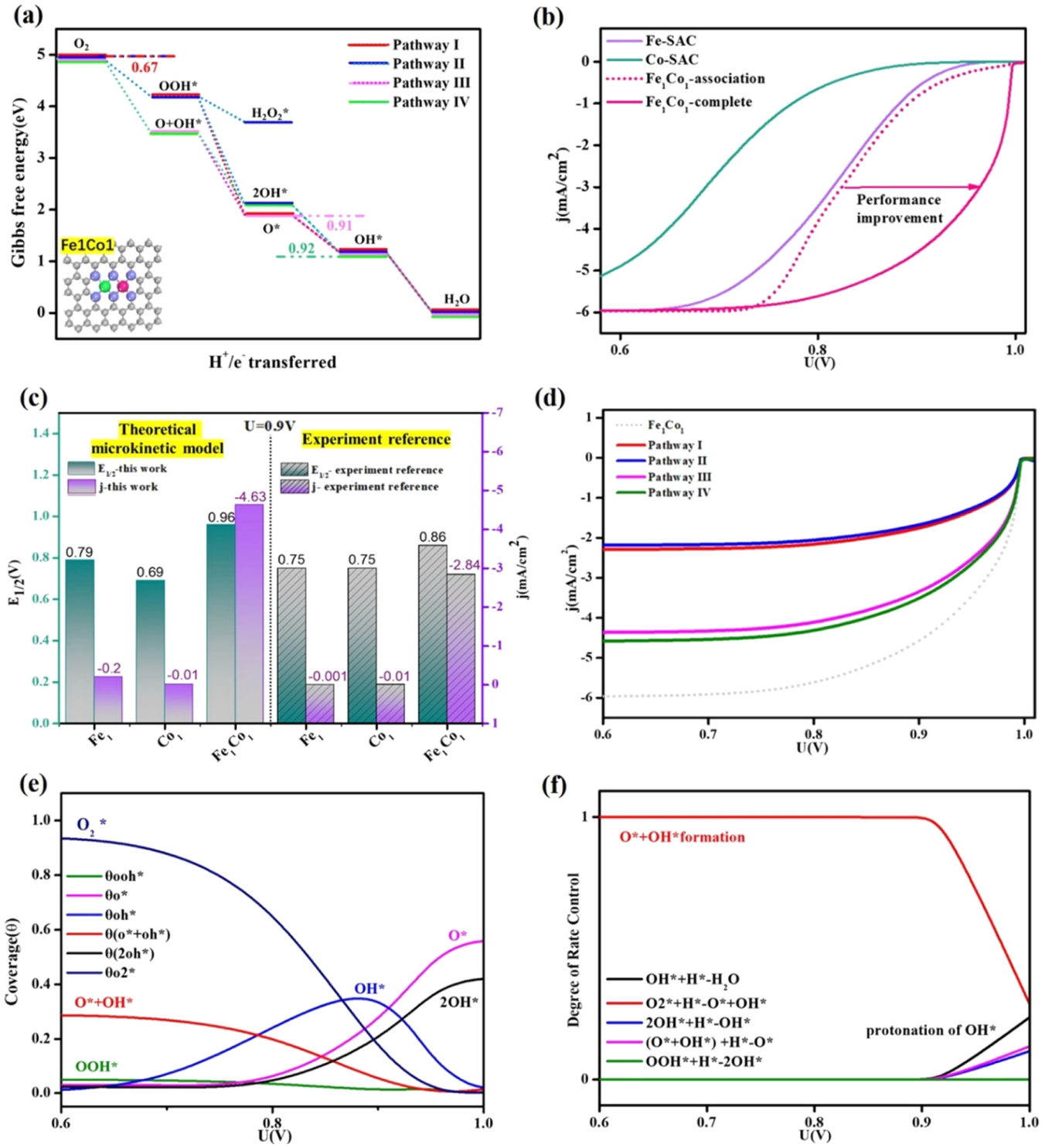

Figure 3. (a) Calculated free energy profiles of reaction pathways I–IV for ORR on Fe_1Co_1-DAC. (b) Simulated polarization curves of Fe/Co-SAC and Fe_1Co_1-DAC through the sole single-site association pathway and complete pathways. (c) Comparison of half-wave potential ($E_{1/2}$, V vs RHE) and current density (mA/cm^2) at 0.9 V versus RHE on Fe_1Co_1-DAC and Fe/Co-SAC between the theoretical microkinetic model and the experiment reference.[69] (d) Simulated polarization curves of Fe_1Co_1-DAC and the contribution from various pathways. (e) The coverage of the intermediate and (f) degree of rate control for each elementary step in the reaction network as a function of output potential on Fe_1Co_1-DAC. Note: coverage and degree of rate control profiles for only the relevant states are shown in the respective panel for each metal, and those not explicitly shown indicate zero coverage.

the competing steps between single-site association and dual-site dissociation mechanisms on Fe_1Co_1-DAC is shown in Figure 2c. O_2* is preferable to be dissociated and hydrogenated simultaneously to O* + OH* with a ΔG of −1.46 eV, which is much lower than that of OOH* formation (ΔG = −0.17 eV). The step OOH* → 2OH* (ΔG = −1.64 eV) is more exothermic than the step OOH* → O* (ΔG = −1.39 eV). In addition to constant-potential calculation, the constant-charge calculation

https://doi.org/10.1021/jacsau.3c00432
JACS Au 2023, 3, 3031−3044

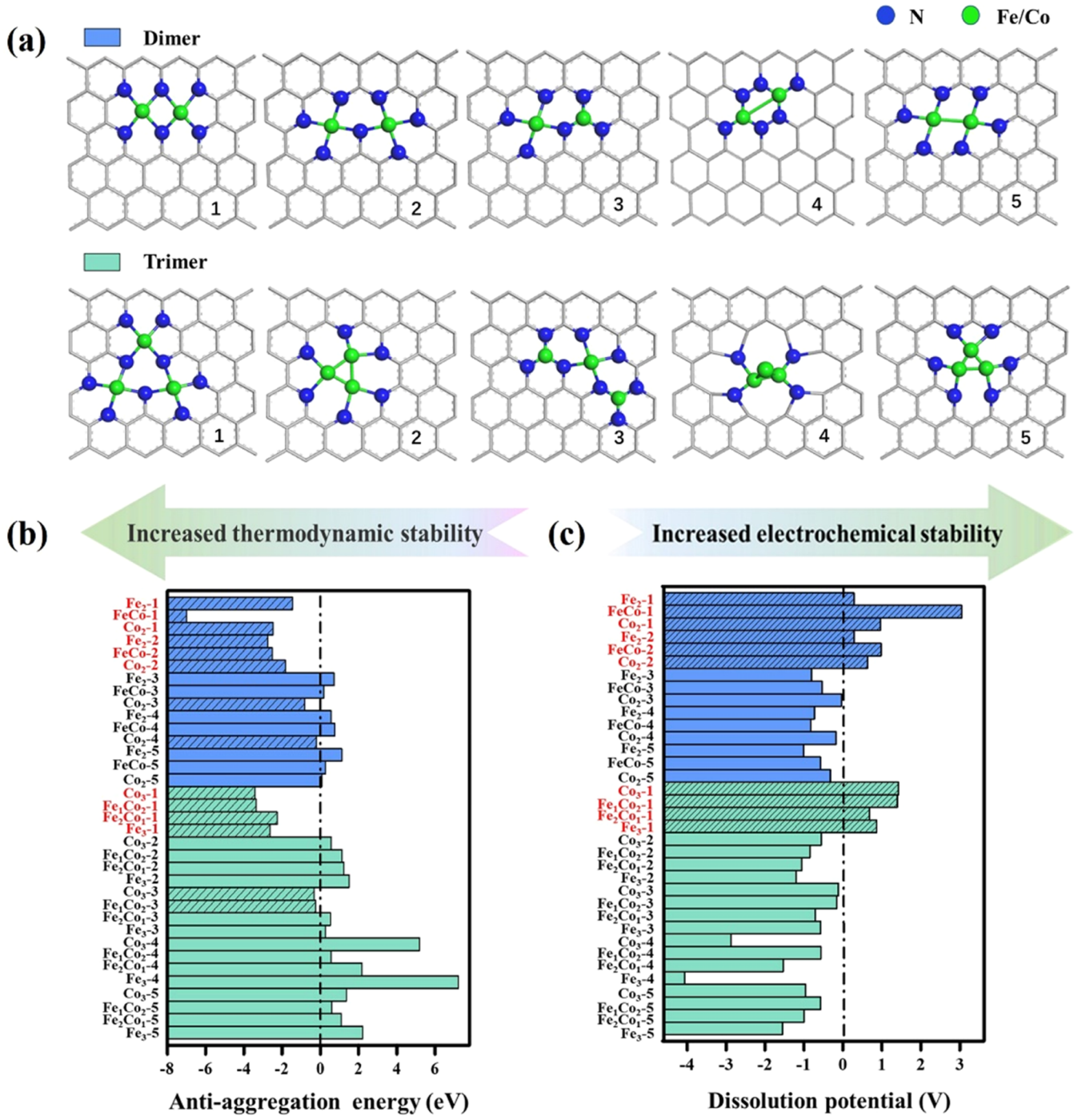

Figure 4. (a) Geometric structures of Fe−Co DACs/TACs with coordination configurations 1−5 (Fe_xCo_{2-x}-1−5-NC/ Fe_xCo_{3-x}-1−5-NC). (b, c) Computed antiaggregation energy and dissolution potential of metal atoms in Fe−Co DACs/TACs, respectively (Fe−Co DACs/TACs with $E_{anti\text{-}agg}$ < 0 eV and $U_{diss} \geq 0$ V vs RHE are marked in red).

also supports the thermodynamic priority of dual-site dissociation mechanisms (Figures 2c and S3). Subsequently, Figures 2d and S4 show that the H-aided O_2 dissociation is more facile than O_2 direct dissociation of the O−O bond for dual-site dissociation mechanisms. Figure 2d and Table S1 also show that the cleavage barrier of the O−O bond upon O_2* + H* into O* + OH* is much lower on Fe_1Co_1-DAC (0.14 eV) than that on Fe-SAC (0.90 eV), and it is also much lower than the associative pathway barrier of O_2* + H* → OOH* on Fe_1Co_1-DAC (0.62 eV). The reason for the facile cleavage of the O−O bond is attributed to the effective activation of the O−O bond on the Fe−Co dual site. Thus, thanks to the dual channel of electron acceptance−backdonation, the dual-site dissociation mechanism shows thermodynamic and kinetic feasibility on DAC and should not be neglected in the ORR network.

3.2. Contribution of Dual-Site Dissociation Pathways for Enhanced ORR Activity

To determine the predominant mechanisms in ORR on DAC/TACs, free energy profiles for Fe_1Co_1-DAC are shown in Figure 3a. ORR is a four-electron reaction, and the onset potential is limited by the step with the smallest free energy drop, which is

https://doi.org/10.1021/jacsau.3c00432
JACS Au 2023, 3, 3031−3044

also the rate-determining step of ORR. A smaller free energy drop in the rate-determining step indicates a lower onset potential for ORR. Based on thermodynamic analysis, the rate-determining step of ORR on pathways III and IV (dissociation mechanism) is identified to be O* → OH*, and ΔG values are −0.91 and −0.92 eV, respectively, much lower than that of pathway I (association mechanism), where ΔG is only −0.67 eV from O_2* to OOH*. Accordingly, the rate-determining steps of pathways III and IV are both more exothermic than that of pathway I, which indicates that the dual-site dissociation mechanism contributes more activity in ORR. Moreover, we perform an electrode microkinetic model to simulate polarization curves (see details in the Supporting Information). For convenience, the rate for electrochemical reduction steps is calculated by assuming an activation energy of 0.26 eV for proton transfers to oxygen-involved intermediates in aqueous solution as previously suggested.[18] In Figure 3b, when Fe_1Co_1-DAC only proceeded through the single-site association mechanism (named Fe_1Co_1-associate), it shows similar ORR activity to Fe-SAC, which is inconsistent with experimental results.[69,72,73] Obviously, when the dual-site dissociation mechanism is considered (named Fe_1Co_1-complete), there is a remarkable ORR performance improvement on Fe_1Co_1-DAC. Attributed to the consideration of complete reaction pathways I−VI, the simulated half-wave potential ($E_{1/2}$) and current density at 0.9 V versus reversible hydrogen electrode (RHE) on Fe_1Co_1-DAC were superior to those on Fe/Co-SAC, which is in good agreement with that reported in experiments (Figure 3c and Table S2).[69] The current density and dominant contribution of the dual-site dissociation pathway were not significantly changed when the calculated barrier of the O−O bond dissociation step rather than 0.26 eV was adopted in the microkinetic model (Figure S4). Thus, the reaction pathway switch to the dual-site dissociation mechanism rationalizes the superior ORR kinetic behavior of Fe_1Co_1-DAC to Fe/Co-SAC.

To further identify the contribution of the dual-site dissociation pathway in the ORR kinetics, we analyze the contribution of each pathway to the total polarization curve for Fe_1Co_1-DAC, as shown in Figure 3d. Obviously, pathway I (red) contributes a little current density, while pathways III (pink) and IV (green) contribute much more degree of flux, indicating that the dual-site dissociation pathway is dominant. In addition, Figure 3e−f shows potential-dependent intermediate coverage and degree of rate control for each elementary step (details of degree of rate control are available in the Supporting Information) for Fe_1Co_1-DAC. The O* + OH* formation from the hydrogenation of O_2*, involved in the dual-site dissociation mechanism, is found to be the rate-limiting step, indicating that ORR proceeds dominantly through the dual-site dissociation pathway. Besides, within the working potential range, the coverage of both O* + OH* and 2OH* intermediates belonging to the dual-site dissociation pathway is much larger than that of OOH* involved in the single-site association pathway. It also suggests a predominant contribution of the dual-site dissociation pathway to ORR activity on Fe_1Co_1-DAC.

3.3. Pathways Switch to the Dual-Site Dissociation Mechanism on DACs/TACs

To further evaluate the feasibility of pathway switch to the dual-site dissociation mechanism on DACs/TACs and its impact on ORR activity, we also employ a thermodynamic and microkinetic model from DFT-derived energetics on other Fe/Co DACs/TACs embedded in N-doped graphene. As shown in Figure 4a, we have constructed a total of 15 Fe−Co DAC (named $Fe_xCo_{(2-x)}$-y-NC, y = 1−5, x = 0−2) and 20 Fe−Co TAC (named $Fe_xCo_{(3-x)}$-y-NC, y = 1−5, x = 0−3) models, in which Fe−Co bi-atoms and tri-atoms are embedded in a N-doped graphene sheet with five different types of environmental coordination. We evaluated the thermodynamic and electrochemical stabilities of these 35 models by the antiaggregation energy ($E_{anti\text{-}agg}$) and dissolution potential (U_{diss}), which are defined as follows.

$$E_{anti\text{-}agg} = E_{Fe_xCo_{2-x}\text{-}NC} - E_{Fe_xCo_{2-x}\text{-}1\text{-}NC} - E_{Fe/Co,bulk} \quad (4)$$

$$U_{diss} = U^0{}_{diss(metal,bulk)} - E_{anti\text{-}agg}/ne \quad (5)$$

where $E_{Fe/Co,bulk}$ is the total energy of the metal atom in its most stable bulk structure, $E_{Fe_xCo_{2-x}\text{-}NC}$ and $E_{Fe_xCo_{2-x}\text{-}1\text{-}NC}$ are the total energies of Fe_xCo_{2-x}-NC and the substrate in which an Fe/Co atom has been dissolved, and $U_{diss}{}^0$ ($U_{Fe}{}^0$ = −0.447V, $U_{Co}{}^0$ = −0.28 V) and n are the standard dissolution potential of the bulk metal and the number of electrons transferring involved in the dissolution, respectively. According to our definition, systems with $E_{anti\text{-}agg} < 0$ eV (for the system containing both Fe and Co atoms, $E_{anti\text{-}agg} = \max[E_{anti\text{-}agg\text{-}Fe}, E_{anti\text{-}agg\text{-}Co}] < 0$) are considered to be thermodynamically stable, while materials with $U_{diss} \geq 0$ V versus RHE are regarded as electrochemically stable. The values of $E_{anti\text{-}agg}$ and U_{diss} are listed in Table S3. Figure 4b shows the $E_{anti\text{-}agg}$ of the heteronuclear Fe−Co DACs/TACs and homonuclear Fe/Co DACs/TACs examined in this study. We finally screened out 10 systems that meet the stability criteria, as shown in Figure 4b,c marked in red. Since stable horizontal adsorption of oxygen molecules on DACs/TACs is a necessary prerequisite for the dual channel of electron acceptance−backdonation mechanism, we studied the adsorption of O_2 on the 10 DACs/TACs that meet the stability criteria. Among them, only O_2 on Co_2-2 DAC cannot be horizontally adsorbed, while the other 9 systems can horizontally adsorb O_2. In some DACs/TACs, horizontal adsorption of O_2 is thermodynamically less favorable than vertical adsorption and is regarded as a high-energy metastable structure. Even though the proportion of O_2 horizontal adsorption may be lower than that of O_2 vertical adsorption throughout the catalytic reaction, it can dictate catalysis with extraordinary activity arising from its unique dual channel for electron acceptance−backdonation mechanism and accordingly dual-site dissociation pathways. The key role of high-energy metastable structure-enabled catalysis has been demonstrated before.[74]

Then, we present and discuss the pre-adsorption phase diagram of 10 stable systems (see details in the Supporting Information), which allows us to analyze the most stable pre-adsorption situation of each system under the operating potential.

$$G = G_{[U=0,pH=0]} - meU \quad (6)$$

A spontaneously absorbed different ORR intermediate (OH*, O*, or O_2*) with the lowest free energy (G) at a given set of potential (U) and pH = 0 determines the stable form of the surface in those conditions. Each intermediate species along the catalytic path for ORR is characterized by a straight line with a negative slope, which is determined by the number of electrons to be transferred. m is the number of electrons to be transferred (1 for m-G(OH*), 2 for m-G(O*), and 4 for m-G(O_2*)). The intermediate corresponding to the lowest line at a common ORR working potential (U = 0.9 V) is regarded as the most

https://doi.org/10.1021/jacsau.3c00432
JACS Au 2023, 3, 3031−3044

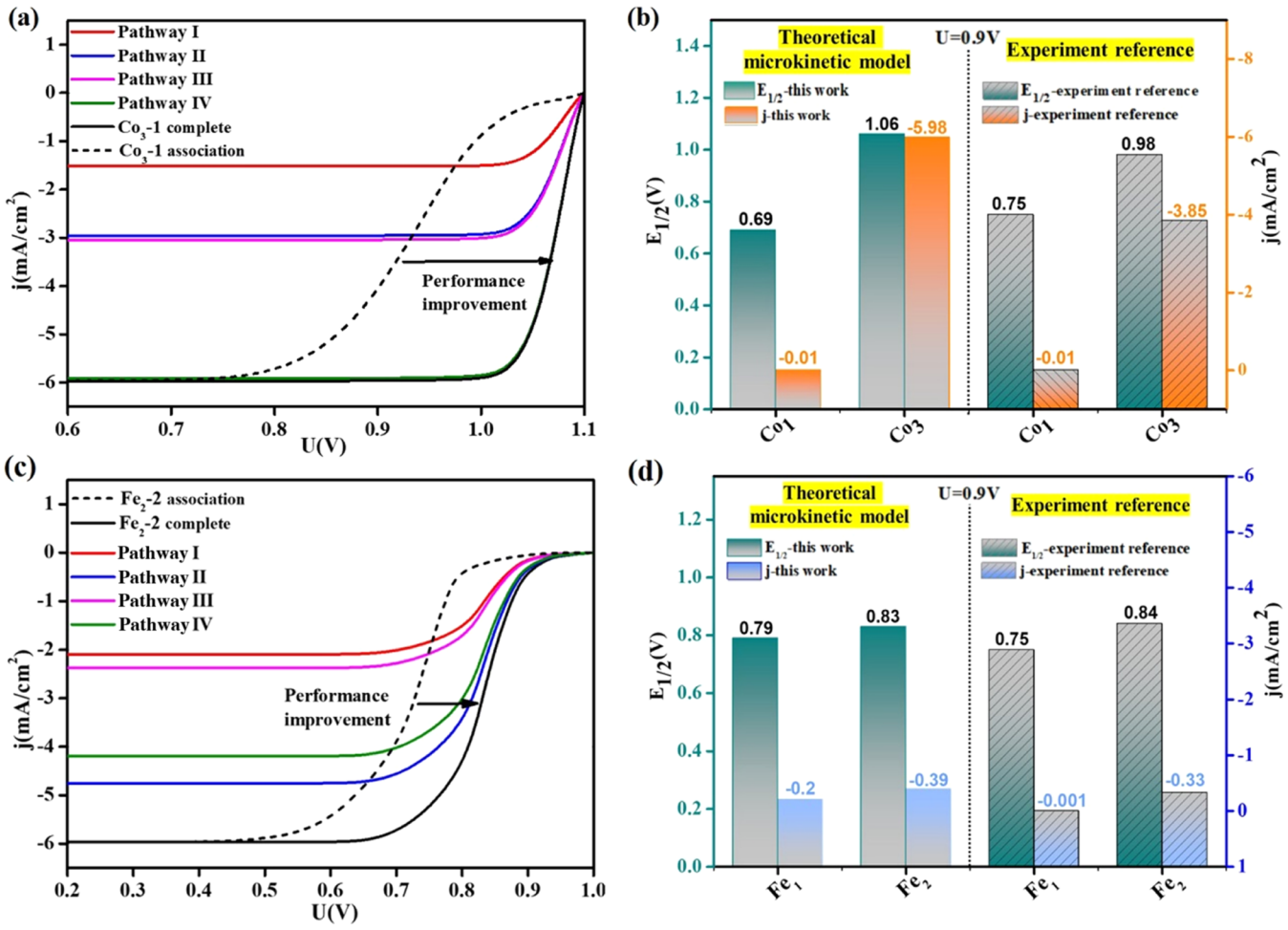

Figure 5. (a) Simulated polarization curves of Co_3-TAC. (b) Comparison of half-wave potential ($E_{1/2}$, V vs RHE) and current density at 0.9 V versus RHE on Co-SAC and Co_3-TAC between the theoretical microkinetic model and the experiment reference.[75] (c) Simulated polarization curves of Fe_2-2 DAC and (d) the simulated $E_{1/2}$ value and j at 0.9 V are in good agreement with those reported in experiments.[23]

stable form in this work. Therefore, the most stable form of 10 stable systems is determined for further study of the reaction mechanism, as shown in Figures S5 and S6. We reveal a potential-dependent structural switching of the active site between planar and non-planar structures during ORR electrocatalysis, which provides important insights, since the axial coordination effect can adjust the electronic structure of the central atom.

Taking Co_3-1 TAC as an example to evaluate the priority of dual-site dissociation mechanisms in a complete ORR network induced by the dual channel of electron acceptance−backdonation. It is apparent that the features of the O−O bond activation of Co_3-1 TAC agree well with those of Fe_1Co_1-DAC, namely, a dual channel of electron acceptance−backdonation is formed, which could be conducive to the sufficient activation of O_2 (Figure S7a). The O−O bond cleavage barrier of Co_3-1 TAC is lower than that of Co-SAC (Figure S7b), which indicates the reasonability of dual-site dissociation mechanisms on Co_3-1 TAC. As shown in Figure 5a, the ORR activity of complete reaction pathways (Co_3-1 complete, black), primarily contributed by dual-site dissociation pathways, is remarkably improved compared with that derived from the sole association pathway (Co_3-1 association, dotted). Therefore, dual-site dissociation pathways rather than the single-site association pathway account for the superior ORR of Co_3 to Co_1 in the experiment.[75] Moreover, 2OH* and OH* are abundant species at the working potential range, accompanied by the hydrogenation of 2OH*(2OH* transfer to OH*) being the second rate-limiting step (Figure S7c,d), which unequivocally indicates that ORR proceeds exclusively through the dual-site dissociation mechanism on Co_3-1 TAC. These results above suggested that the reaction pathway switch to the dual-site dissociation pathway rationalizes the superior kinetic behavior of Co_3-1 TACs to Co-SAC.

The dual-site dissociation mechanism is still observed on Fe_2-2 DAC. Within the working potential range, the coverage of the 2OH* intermediate belonging to the dual-site dissociation pathway is much larger than that of OOH* involved in the single-site association pathway (Figure S8). Besides, the ORR activity of the complete reaction pathway (Fe_2-2 complete, black), which is mainly contributed by the dual-site dissociation pathway, is significantly higher than that of the single association pathway (Fe_2-2 association, dotted), as shown in Figure 5c. Due to the involvement of the dual-site dissociation pathway in the reaction network, the half-wave potential of Fe_2-2 increases relative to that of Fe_1-SAC, rationalizing the superior kinetic behavior of Fe_2-2 DACs to Fe-SAC in the experiment[23,61,62] (Figure 5d). Likewise, the consideration of the dual-site dissociation mechanism increases the onset potential or the half-wave potential (Figure S10 and Tables S4 and S5) of the

https://doi.org/10.1021/jacsau.3c00432
JACS Au 2023, 3, 3031−3044

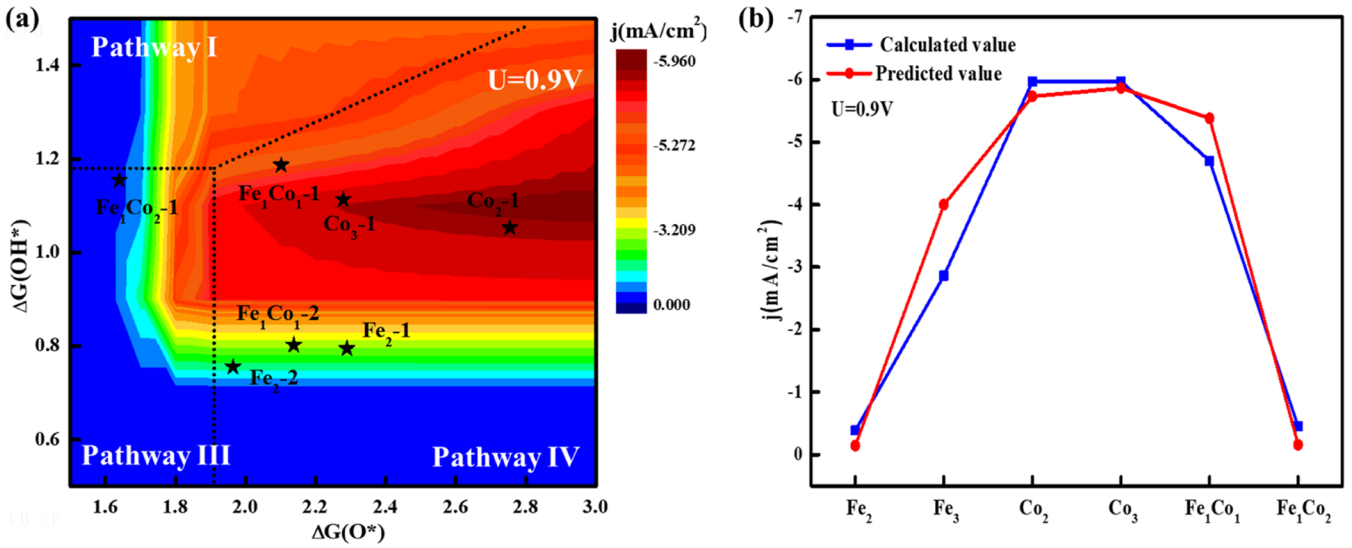

Figure 6. Contour plot of current density at electrode potentials of 0.9 V versus RHE as a function of $\Delta G(O^*)$ and $\Delta G(OH^*)$ accompanied by the reaction pathway phase diagram. (b) The comparison between predicted and computed current densities at 0.9 V versus RHE.

other 8 FeCo DACs/TACs systems compared with the single-site association pathway. Although the barrier of O_2 dissociation upon hydrogenation by surface H* on Fe_2-2 DAC is not as favorable as Fe_1Co_1-1 DAC and Co_3-1 TAC (Table S1), when the energy barrier of O_2 dissociation was brought into the microkinetic model, it was found that the polarization curve changes little and the dual-site dissociation path is still dominant (Figure S5), which indicate that the direct hydrogenation of O_2 by surface H* or solvent proton does not affect the conclusion of this study. Dual-site dissociation pathways rather than the single-site association pathway contribute most of the current flux in ORR, which suggests the reliability and feasibility of pathway switch in the ORR network for DACs/TACs. Although the metal active center and environmental coordination configurations of these DACs/TACs systems are different, the ORR mechanisms possess fairly similar features, implying that the presence of adjacent metal sites on DACs/TACs plays a key role in ORR pathway switch to the dual-site dissociation mechanism. We note that the limitation of CHE modeling applied here is to consider the pH effect on the reactivity of catalysts, since the free energy correction of the pH effect is offset when the potentials are regulated to the reversible hydrogen electrode (RHE) scale. The pH effect on the adsorption behavior of intermediates, which leads to the difference in the ORR activity of ADMCs on acidic and alkaline media, will be considered in our future work by using grand canonical ensemble DFT.[54,76]

3.4. Reaction Phase Diagram and Activity Trend of ORR on DACs/TACs

The theoretical prediction of the catalytic activity trend has been widely focused on due to its significant value in providing a guideline for a catalyst design, where the complete consideration of the reaction pathway is essential. Based on the identified dual-site dissociation pathway and the revised ORR network in Figure 1c, a new reaction phase diagram (RPD) of complete ORR pathways I–VI can be constructed to predict the pathway priority and activity trend in this work among DACs/TACs. The free energies of OOH*, O* + OH*, O*, 2OH*, and OH* on $10Fe_xCo_{2-x}$-NC/Fe_xCo_{3-x}-NC systems are calculated and plotted in Figure S11. The DFT adsorption energies, zero-point energies, entropy, and solvation corrections needed to calculate free energies are available in Table S6, and the structure configurations are shown in Figure S12. The scaling relations between $\Delta G(OH^*)$, $\Delta G(O^*)$, and $\Delta G(OOH^*)$ are still applicable in these systems, which are in good agreement with previous reports.[28,40,77] Importantly, two new scaling relations are identified for 2OH* and O* + OH* adsorbed on adjacent active sites

$$\Delta G(O^* + OH^*) = 0.16\Delta G(O^*) + 0.78\Delta G(OH^*) \quad (7)$$

$$\Delta G(2OH^*) = 0.3\Delta G(O^*) + 0.46\Delta G(OH^*) \quad (8)$$

The $\Delta G(OH^*)$ term represents the free energy of a single OH* adsorbed on the active site, and the $\Delta G(2OH^*)$ term represents the free energy of two OH* adsorbed on adjacent Fe–Co sites. In other words, $\Delta G(2OH^*)$ is not equal to $2\Delta G(OH^*)$ on Fe–Co DACs/TACs with adjacent active sites, as two OH* can bond to different active sites and have an effect on the free energy of each other. In the same way, the free energy of O* + OH* is no longer thermodynamically equivalent to $\Delta G(OH^*)$ + $\Delta G(O^*)$. Since the free adsorption energy of each intermediate shows scaling relations with the combination between $\Delta G(O^*)$ and $\Delta G(OH^*)$ (Figure S12a), the free energy change of each elementary step along ORR pathways I–VI is relationally correlated with $\Delta G(O^*)$ and $\Delta G(OH^*)$, as shown in Figure S12b–e. As the adsorption free energies of $\Delta G(O^*)$ and $\Delta G(OH^*)$ show a good linear relationship with each parameter in ORR kinetics, $\Delta G(O^*)$ and $\Delta G(OH^*)$ are chosen as independent variables to evaluate the trend of preferential ORR pathways and ORR activity. A more accurate consideration of both catalytic mechanisms and the prediction of the activity trend can be conducted by a collective description of complete reaction pathways, named the reaction phase diagram (RPD) for simplicity in this work. The ORR current density on different catalysts with a given value of the descriptor ($\Delta G(O^*)$, $\Delta G(OH^*)$), $j_{RPD}(\Delta G(O^*), \Delta G(OH^*))$ is determined by the following expression

$$j_{RPD}(\Delta G(O^*), \Delta G(OH^*)) = \max_i[e\rho TOFe^-] \quad (9)$$

where all possible reaction pathways (denoted i) are established, considering all forward and backward elementary steps. e is the

https://doi.org/10.1021/jacsau.3c00432
JACS Au 2023, 3, 3031–3044

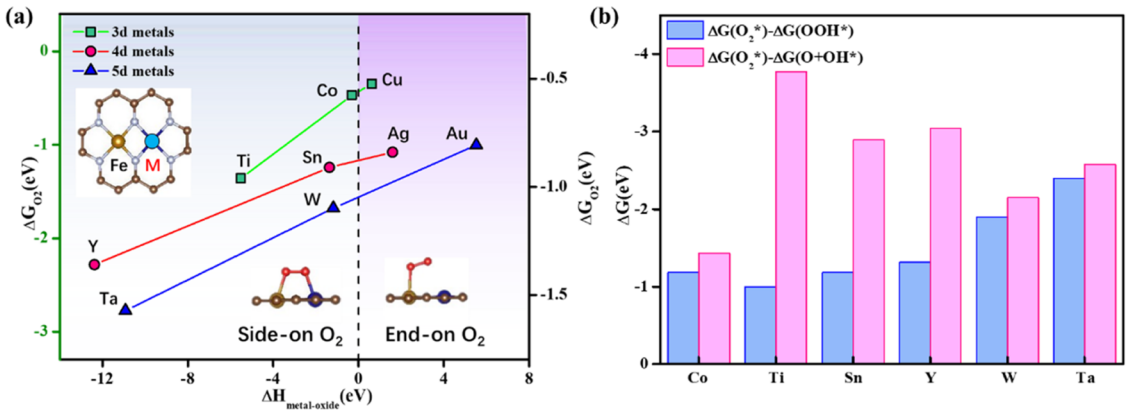

Figure 7. (a) Correlation between oxygen adsorption energy (ΔG_{O_2}) and the $\Delta H_{metal\text{-}oxide}$ of M of FeM-DACs. (b) The reaction free energy of the competing steps between single-site association and dual-site dissociation pathways on FeM-DACs.

elementary charge, ρ is the surface density of active sites, and $TOFe^{-}$ is the turnover frequency of electron transfer. All considered pathways are compared to each other to identify one contributing the highest current density to the total ORR. As shown in Figure 6a, a reaction phase diagram at the electrode potential of 0.9 V versus RHE is established, where the predominant reaction pathways can be derived from the RPD at various given O* and OH* free energies. We find in this work that an ideal catalyst possessing high ORR activity is in the range of $\Delta G(O^*)$ = 2.4−3.0 eV and $\Delta G(OH^*)$ = 1−1.2 eV. Pathway IV is more favored over Fe_1Co_1-1, Fe_1Co_1-2, Fe_2-1, Fe_2-2, Co_2-1, Co_2-2, and Co_3-1, and pathway III is more preferred on Fe_1Co_2-1, which suggests that DACs/TACs are more likely to follow the dual-site dissociation mechanism. The comparison between the predicted ORR activity and the DFT-calculated ones shows an excellent agreement (Figure 6b), which also illustrates the prediction accuracy of the three-dimensional volcano plot spanned by the adsorption free energies of $\Delta G(O^*)$ and $\Delta G(OH^*)$.

Understanding how the electronic characteristics of the active center affect $\Delta G(O^*)$ and $\Delta G(OH^*)$ helps to guide the modification of the DAC/TAC active center and makes them closer to the volcanic summit. Taking the Fe active center in FeCo DACs/TACs as an example, Figure S13a shows the d-electron configurations of iron cations. The iron cations are regarded as +3 valence based on Bader charges analysis in Figure S14. The stable spin configurations of +3 valence iron cations may be in the intermediate-spin state and low-spin state. The intermediate-spin state of Fe^{3+} enables t_{2g} and e_g orbitals to be occupied by one unpaired electron with two and single spin, making the whole d-shell act as selective gates to promote the transfer of local spin currents. The calculated effective magnetic moments of Fe_1Co_1-1 and Fe_2-2 are 3.77 μ_{eff} and 2.48 μ_{eff}, respectively. We further obtained the number of unpaired d-electrons (n) of Fe^{3+} ion via the following equation

$$\mu_{eff} = \sqrt{n \times (n+2)} \tag{10}$$

where the number of unpaired d-electrons (n) of Fe_2-2 is about 1.67, which means Fe^{3+} ions have a low-spin state without e_g filling, so that no electron is occupied in the σ^* antibonding orbital of Fe_2-2, leading to a relatively stronger Fe/OH* interaction (a bond order of 2, Figure S13c). The number of unpaired d-electrons (n) of Fe_1Co_1-1 is about 3, which indicates an intermediate magnetic moment of the Fe center and the orbital interaction with *OH resulting in a lower bond order of 1.5 (Figure S13b). Since a higher on-site magnetic moment of the Fe center leads to a lower value of bond order, representing a weaker chemical bond strength, a positively linear correlation is reasonably found between $\Delta G(OH^*)$ and the on-site magnetic moment of the Fe center (Figure S13d), clearly indicating that the spin configurations on the Fe center are the intrinsic factor dominating the ORR activity.

3.5. ORR Pathway Conversion on Other DACs

In addition to FeCo DACs/TACs supported on N-doped graphene, other metal elements or other substrates for ADMCs, such as RuCo-graphene[78] and FePt-oxide,[79] have also been reported exhibiting high ORR activity. Thus, we investigate the applicability of pathway switch from the single-site associative mechanism to the dual-site dissociation mechanism on the $PtFe@Fe_2O_3(012)$[79] surface and RuCo@graphene.[78] A comprehensive analysis of the calculation results shows that the oxygen molecules can be adsorbed separately on the appropriately distanced Pt and Fe atoms of $PtFe@Fe_2O_3(012)$, forming a dual channel of electron acceptance−backdonation, which could directly catalyze O−O radical breakage and cause the ORR to follow a fast-kinetic dual-site dissociation mechanism. As shown in Figure S15, the current densities (j) of pathways III (pink −3.39 mA cm^{-2}) and IV (green −5.56 mA cm^{-2}) are closer to the total current density (dotted line −5.97 mA cm^{-2}), indicating that the dual-site dissociation pathway is dominant. Moreover, the dual-site dissociation mechanism brings about better and reasonable onset potentials (E_{onset} = 1.17 V), which is in better agreement with the one (E_{onset} = 1.15 V) obtained in experiments, compared to the single-site associative mechanism (E_{onset} = 0.75 V).[79] The features of the O−O bond activation on RuCo@graphene agrees well with that on $PtFe@Fe_2O_3$, and the ORR mechanisms possess fairly similar features, implying that the domination of the dual-site dissociation pathway is still applicable in this system.

Since the dual-site dissociation pathway of ORR requires two adsorption sites for oxygen-involved intermediates, we inferred that the oxyphilic property of the metal site might be an important factor in determining the feasibility of the dual-site dissociation pathway. Campbell et al.[80] demonstrated that the enthalpy of oxidation formation of metal adsorptive atoms can be used to effectively evaluate the oxygen-affinity ability of metal elements, which has been further validated in recent experiments and calculations.[81] Therefore, three metal elements with large differences in the enthalpy of oxidation formation

https://doi.org/10.1021/jacsau.3c00432
JACS Au 2023, 3, 3031−3044

($\Delta H_{metal\text{-}oxide}$)[82] in the fourth, fifth, and sixth rows of the periodic table were selected to form FeM-DACs supported on N-doped graphene (M = Ti, Co, Cu, Y, Zn, Ag, Au, W, and Ta; Figure 7). As shown in Figure 7a, in the case of $\Delta H_{metal\text{-}oxide} \geq 0$ of M, O_2 cannot be horizontally adsorbed in the corresponding FeM-DACs after structural relaxation, that is, they cannot go through the dual channel for electron acceptance−backdonation mechanism. In the case of $\Delta H_{metal\text{-}oxide}$ of $M < 0$, O_2 can bind FeM-DACs with side-on adsorption mode. Thanks to the dual channel for electron acceptance−backdonation mechanism, these FeM-DACs allowing O_2 side-on adsorption all show the thermodynamic priority of the dual-site dissociation pathway to the single-site association pathway (Figure 7b). Therefore, we come up with a general insight into the ORR mechanism switch from SACs to DACs/TAC that $\Delta H_{metal\text{-}oxide}$ of metal elements at the dual adjacent sites of DACs/TACs may be an efficient descriptor to judge the feasibility of the side-on adsorption mode of O_2 and the dual-site dissociation pathway.

Thus, dual-site dissociation pathways involving O−O breakage during ORR should not be overlooked in the future rational design of DACs/TACs. Besides, this work also indicates that the enhancement of a dual channel for electron acceptance−backdonation on DACs/TACs is a promising approach to efficiently promote O−O bond breakage, accordingly improving the ORR activity due to the reaction pathway switch.

4. CONCLUSIONS

In summary, we propose the "dual channel for electron acceptance−backdonation" mechanism to rationalize the more activation of the O−O bond on Fe_1Co_1-DAC than Fe-SAC, which makes ORR switch to proceed through dual-site dissociation pathways from the traditional single-site association pathway. According to the polarization curve calculated by the DFT-based microkinetic model, the ORR activity of complete reaction pathways, primarily contributed by dual-site dissociation pathways, is remarkably improved compared with that derived from the sole association pathway. To further evaluate the feasibility of pathway switch to the dual-site dissociation mechanism on DACs/TACs and its impact on ORR activity, we have constructed a total of 15 Fe−Co DAC and 20 Fe−Co TAC models embedded in N-doped graphene. Although the metal active center and environmental coordination configurations of these DACs/TACs systems are different, the preferential ORR pathway possesses fairly similar features. Following this revised ORR network, a complete reaction phase diagram of DACs/TACs is established, where the preferential ORR pathway and ORR activity can be described by a three-dimensional volcano plot spanned by the adsorption free energies of $\Delta G(O^*)$ and $\Delta G(OH^*)$. Besides, the kinetics preferability of dual-site dissociation pathways is also appropriate for other graphene-supported or oxide-supported DACs/TACs. The contribution of dual-site dissociation pathways makes the theoretical ORR activity of DACs/TACs in better agreement with the available experiment than the traditional single-site association pathway, rationalizing the superior kinetic behavior of DACs/TACs to SACs. The enthalpy of oxidation formation ($\Delta H_{metal\text{-}oxide}$) of the metal element at the double adjacent sites of DACs/TAC is found as an effective descriptor to judge the feasibility of the side-on adsorption mode of O_2 and the dual-site dissociation pathway. This work reveals the origin of ORR pathway switching from SACs to DACs/TACs and indicates that dual-site dissociation pathways during ORR should not be overlooked in the rational design of DACs/TACs.

ASSOCIATED CONTENT

Supporting Information

The Supporting Information is available free of charge at https://pubs.acs.org/doi/10.1021/jacsau.3c00432.

Pathway of the oxygen reduction reaction (ORR); structures and adsorption energies of reactants, intermediates, transition states, and products; comparison of predicted and calculated results about the polarization curves; and analyses related to the O_2* adsorption energy, microkinetic models, energy descriptor to regulate reaction pathways I−IV for ORR (PDF)

AUTHOR INFORMATION

Corresponding Author

Daojian Cheng − *State Key Laboratory of Organic−Inorganic Composites, Interdisciplinary Research Center for hydrogen energy, Beijing University of Chemical Technology, 100029 Beijing, People's Republic of China*; orcid.org/0000-0001-7977-0750; Email: chengdj@mail.buct.edu.cn

Authors

Jin Liu − *State Key Laboratory of Organic−Inorganic Composites, Interdisciplinary Research Center for hydrogen energy, Beijing University of Chemical Technology, 100029 Beijing, People's Republic of China*

Haoxiang Xu − *State Key Laboratory of Organic−Inorganic Composites, Interdisciplinary Research Center for hydrogen energy, Beijing University of Chemical Technology, 100029 Beijing, People's Republic of China*

Jiqin Zhu − *State Key Laboratory of Chemical Resource Engineering, Beijing University of Chemical Technology, 100029 Beijing, People's Republic of China*

Complete contact information is available at: https://pubs.acs.org/10.1021/jacsau.3c00432

Author Contributions

[§]J.L. and H.X. contributed equally to this work. CRediT: **Jin Liu** writing-original draft; **Haoxiang Xu** supervision, writing-review & editing.

Notes

The authors declare no competing financial interest.

ACKNOWLEDGMENTS

This work is supported by the National Key Research and Development Program of China (2021YFA1500501) and the National Natural Science Foundation of China (21975016 and 22005025).

REFERENCES

(1) Chen, Z. W.; Chen, L. X.; Yang, C. C.; Jiang, Q. Atomic (single, double, and triple atoms) catalysis: frontiers, opportunities, and challenges. *J. Mater. Chem. A* **2019**, *7*, 3492−3515.

(2) Liu, M.; Wang, L.; Zhao, K.; Shi, S.; Shao, Q.; Zhang, L.; Sun, X.; Zhao, Y.; Zhang, J. Atomically dispersed metal catalysts for the oxygen reduction reaction: synthesis, characterization, reaction mechanisms and electrochemical energy applications. *Energy Environ. Sci.* **2019**, *12*, 2890−2923.

(3) Yang, X. F.; Wang, A.; Qiao, B.; Li, J.; Liu, J.; Zhang, T. Single-atom catalysts: a new frontier in heterogeneous catalysis. *Acc. Chem. Res.* **2013**, *46*, 1740−1748.

(4) Chen, Y.; Ji, S.; Chen, C.; Peng, Q.; Wang, D.; Li, Y. Single-Atom Catalysts: Synthetic Strategies and Electrochemical Applications. *Joule* **2018**, *2*, 1242−1264.
(5) Wang, J.; Li, Z.; Wu, Y.; Li, Y. Fabrication of Single-Atom Catalysts with Precise Structure and High Metal Loading. *Adv. Mater.* **2018**, *30*, No. 1801649.
(6) Jiao, J.; Lin, R.; Liu, S.; Cheong, W. C.; Zhang, C.; Chen, Z.; Pan, Y.; Tang, J.; Wu, K.; Hung, S. F.; Chen, H. M.; Zheng, L.; Lu, Q.; Yang, X.; Xu, B.; Xiao, H.; Li, J.; Wang, D.; Peng, Q.; Chen, C.; Li, Y. Copper atom-pair catalyst anchored on alloy nanowires for selective and efficient electrochemical reduction of CO2. *Nat. Chem.* **2019**, *11*, 222−228.
(7) Pan, Y.; Zhang, C.; Liu, Z.; Chen, C.; Li, Y. Structural Regulation with Atomic-Level Precision: From Single-Atomic Site to Diatomic and Atomic Interface Catalysis. *Matter* **2020**, *2*, 78−110.
(8) Zhang, J.; Huang, Q.-a.; Wang, J.; Wang, J.; Zhang, J.; Zhao, Y. Supported dual-atom catalysts: Preparation, characterization, and potential applications. *Chin. J. Catal.* **2020**, *41*, 783−798.
(9) Zhou, X.; Han, K.; Li, K.; Pan, J.; Wang, X.; Shi, W.; Song, S.; Zhang, H. Dual-Site Single-Atom Catalysts with High Performance for Three-Way Catalysis. *Adv. Mater.* **2022**, *34*, No. 2201859.
(10) Yan, H.; Lin, Y.; Wu, H.; Zhang, W.; Sun, Z.; Cheng, H.; Liu, W.; Wang, C.; Li, J.; Huang, X.; Yao, T.; Yang, J.; Wei, S.; Lu, J. Bottom-up precise synthesis of stable platinum dimers on graphene. *Nat. Commun.* **2017**, *8*, No. 1070.
(11) Liu, J. C.; Ma, X. L.; Li, Y.; Wang, Y. G.; Xiao, H.; Li, J. Heterogeneous Fe3 single-cluster catalyst for ammonia synthesis via an associative mechanism. *Nat. Commun.* **2018**, *9*, No. 1610.
(12) Xie, P.; Ding, J.; Yao, Z.; Pu, T.; Zhang, P.; Huang, Z.; Wang, C.; Zhang, J.; Zecher-Freeman, N.; Zong, H.; Yuan, D.; Deng, S.; Shahbazian-Yassar, R.; Wang, C. Oxo dicopper anchored on carbon nitride for selective oxidation of methane. *Nat. Commun.* **2022**, *13*, No. 1375.
(13) Yang, Y.; Qian, Y.; Li, H.; Zhang, Z.; Mu, Y.; Do, D.; Zhou, B.; Dong, J.; Yan, W.; Qin, Y.; Fang, L.; Feng, R.; Zhou, J.; Zhang, P.; Dong, J.; Yu, G.; Liu, Y.; Zhang, X.; Fan, X. O-coordinated W-Mo dual-atom catalyst for pH-universal electrocatalytic hydrogen evolution. *Sci. Adv.* **2020**, *6*, No. eaba6586.
(14) Liu, J. C.; Xiao, H.; Li, J. Constructing High-Loading Single-Atom/Cluster Catalysts via an Electrochemical Potential Window Strategy. *J. Am. Chem. Soc.* **2020**, *142*, 3375−3383.
(15) Zhang, L.; Si, R.; Liu, H.; Chen, N.; Wang, Q.; Adair, K.; Wang, Z.; Chen, J.; Song, Z.; Li, J.; Banis, M. N.; Li, R.; Sham, T. K.; Gu, M.; Liu, L. M.; Botton, G. A.; Sun, X. Atomic layer deposited Pt-Ru dual-metal dimers and identifying their active sites for hydrogen evolution reaction. *Nat. Commun.* **2019**, *10*, No. 4936.
(16) Li, Z.; Li, B.; Hu, Y.; Wang, S.; Yu, C. Highly-dispersed and high-metal-density electrocatalysts on carbon supports for the oxygen reduction reaction: from nanoparticles to atomic-level architectures. *Mater. Adv.* **2022**, *3*, 779−809.
(17) Viswanathan, V.; Hansen, H. A.; Rossmeisl, J.; Norskov, J. K. Unifying the 2e(-) and 4e(-) Reduction of Oxygen on Metal Surfaces. *J. Phys. Chem. Lett.* **2012**, *3*, 2948−2951.
(18) Tripković, V.; Skúlason, E.; Siahrostami, S.; Nørskov, J. K.; Rossmeisl, J. The oxygen reduction reaction mechanism on Pt(111) from density functional theory calculations. *Electrochim. Acta* **2010**, *55*, 7975−7981.
(19) Russell, A. E. Electrocatalysis: theory and experiment at the interface. Preface. *Faraday Discuss.* **2008**, *140*, 9−10.
(20) Karlberg, G. S.; Rossmeisl, J.; Nørskov, J. K. Estimations of electric field effects on the oxygen reduction reaction. *Phys. Chem. Chem. Phys.* **2007**, *9*, 5158−5161.
(21) Greeley, J.; Nørskov, J. K. Combinatorial Density Functional Theory-Based Screening of Surface Alloys for the Oxygen Reduction Reaction. *J. Phys. Chem. C* **2009**, *113*, 4932−4939.
(22) Xiao, M.; Zhang, H.; Chen, Y.; Zhu, J.; Gao, L.; Jin, Z.; Ge, J.; Jiang, Z.; Chen, S.; Liu, C.; Xing, W. Identification of binuclear Co2N5 active sites for oxygen reduction reaction with more than one magnitude higher activity than single atom CoN4 site. *Nano Energy* **2018**, *46*, 396−403.
(23) Ye, W.; Chen, S.; Lin, Y.; Yang, L.; Chen, S.; Zheng, X.; Qi, Z.; Wang, C.; Long, R.; Chen, M.; Zhu, J.; Gao, P.; Song, L.; Jiang, J.; Xiong, Y. Precisely Tuning the Number of Fe Atoms in Clusters on N-Doped Carbon toward Acidic Oxygen Reduction Reaction. *Chem* **2019**, *5*, 2865−2878.
(24) Bezerra, C. W. B.; Zhang, L.; Lee, K.; Liu, H.; Marques, A. L. B.; Marques, E. P.; Wang, H.; Zhang, J. A review of Fe−N/C and Co−N/C catalysts for the oxygen reduction reaction. *Electrochim. Acta* **2008**, *53*, 4937−4951.
(25) Zhao, C. X.; Li, B. Q.; Liu, J. N.; Zhang, Q. Intrinsic Electrocatalytic Activity Regulation of M-N-C Single-Atom Catalysts for the Oxygen Reduction Reaction. *Angew. Chem., Int. Ed.* **2021**, *60*, 4448−4463.
(26) Feng, Y.; Alonso-Vante, N. Nonprecious metal catalysts for the molecular oxygen-reduction reaction. *physica status solidi (b)* **2008**, *245*, 1792−1806.
(27) Jiao, L.; Zhu, J.; Zhang, Y.; Yang, W.; Zhou, S.; Li, A.; Xie, C.; Zheng, X.; Zhou, W.; Yu, S. H.; Jiang, H. L. Non-Bonding Interaction of Neighboring Fe and Ni Single-Atom Pairs on MOF-Derived N-Doped Carbon for Enhanced CO2 Electroreduction. *J. Am. Chem. Soc.* **2021**, *143*, 19417−19424.
(28) Kulkarni, A.; Siahrostami, S.; Patel, A.; Norskov, J. K. Understanding Catalytic Activity Trends in the Oxygen Reduction Reaction. *Chem. Rev.* **2018**, *118*, 2302−2312.
(29) Wei, B.; Fu, Z.; Legut, D.; Germann, T. C.; Du, S.; Zhang, H.; Francisco, J. S.; Zhang, R. Rational Design of Highly Stable and Active MXene-Based Bifunctional ORR/OER Double-Atom Catalysts. *Adv. Mater.* **2021**, *33*, No. 2102595.
(30) Xu, J.; Elangovan, A.; Li, J.; Liu, B. Graphene-Based Dual-Metal Sites for Oxygen Reduction Reaction: A Theoretical Study. *J. Phys. Chem. C* **2021**, *125*, 2334−2344.
(31) Zhang, L.; Guo, X.; Zhang, S.; Huang, S. Building up the "Genome" of bi-atom catalysts toward efficient HER/OER/ORR. *J. Mater. Chem. A* **2022**, *10*, 11600−11612.
(32) Zhao, X.; Liu, X.; Huang, B.; Wang, P.; Pei, Y. Hydroxyl group modification improves the electrocatalytic ORR and OER activity of graphene supported single and bi-metal atomic catalysts (Ni, Co, and Fe). *J. Mater. Chem. A* **2019**, *7*, 24583−24593.
(33) Zhu, X.; Yan, J.; Gu, M.; Liu, T.; Dai, Y.; Gu, Y.; Li, Y. Activity Origin and Design Principles for Oxygen Reduction on Dual-Metal-Site Catalysts: A Combined Density Functional Theory and Machine Learning Study. *J. Phys. Chem. Lett.* **2019**, *10*, 7760−7766.
(34) Liu, C.; Li, T.; Dai, X.; Zhao, J.; He, D.; Li, G.; Wang, B.; Cui, X. Catalytic Activity Enhancement on Alcohol Dehydrogenation via Directing Reaction Pathways from Single- to Double-Atom Catalysis. *J. Am. Chem. Soc.* **2022**, *144*, 4913−4924.
(35) Ren, W.; Tan, X.; Yang, W.; Jia, C.; Xu, S.; Wang, K.; Smith, S. C.; Zhao, C. Isolated Diatomic Ni-Fe Metal-Nitrogen Sites for Synergistic Electroreduction of CO2. *Angew. Chem., Int. Ed.* **2019**, *58*, 6972−6976.
(36) Tian, S.; Fu, Q.; Chen, W.; Feng, Q.; Chen, Z.; Zhang, J.; Cheong, W. C.; Yu, R.; Gu, L.; Dong, J.; Luo, J.; Chen, C.; Peng, Q.; Draxl, C.; Wang, D.; Li, Y. Carbon nitride supported Fe2 cluster catalysts with superior performance for alkene epoxidation. *Nat. Commun.* **2018**, *9*, No. 2353.
(37) Xing, D.-H.; Xu, C.-Q.; Wang, Y.-G.; Li, J. Heterogeneous Single-Cluster Catalysts for Selective Semihydrogenation of Acetylene with Graphdiyne-Supported Triatomic Clusters. *J. Phys. Chem. C* **2019**, *123*, 10494−10500.
(38) Xie, Y.; Chen, X.; Sun, K.; Zhang, J.; Lai, W. H.; Liu, H.; Wang, G. Direct Oxygen-Oxygen Cleavage through Optimizing Interatomic Distances in Dual Single-atom Electrocatalysts for Efficient Oxygen Reduction Reaction. *Angew. Chem., Int. Ed.* **2023**, *62*, No. e202301833.
(39) Zhou, W.; Su, H.; Cheng, W.; Li, Y.; Jiang, J.; Liu, M.; Yu, F.; Wang, W.; Wei, S.; Liu, Q. Regulating the scaling relationship for high catalytic kinetics and selectivity of the oxygen reduction reaction. *Nat. Commun.* **2022**, *13*, No. 6414.

https://doi.org/10.1021/jacsau.3c00432
JACS Au 2023, 3, 3031−3044

(40) Zhong, L.; Li, S. Unconventional Oxygen Reduction Reaction Mechanism and Scaling Relation on Single-Atom Catalysts. *ACS Catal.* **2020**, *10*, 4313−4318.
(41) Li, F.; Liu, X.; Chen, Z. 1 + 1′ ≥ 2: Heteronuclear Biatom Catalyst Outperforms Its Homonuclear Counterparts for CO Oxidation. *Small Methods* **2019**, *3*, No. 1800480.
(42) Chen, Z. W.; Yan, J. M.; Jiang, Q. Single or Double: Which Is the Altar of Atomic Catalysts for Nitrogen Reduction Reaction? *Small Methods* **2019**, *3*, No. 1800291.
(43) Han, X.; Ling, X.; Yu, D.; Xie, D.; Li, L.; Peng, S.; Zhong, C.; Zhao, N.; Deng, Y.; Hu, W. Atomically Dispersed Binary Co-Ni Sites in Nitrogen-Doped Hollow Carbon Nanocubes for Reversible Oxygen Reduction and Evolution. *Adv. Mater.* **2019**, *31*, No. 1905622.
(44) Kresse, G.; Furthmüller, J. Efficiency of ab-initio total energy calculations for metals and semiconductors using a plane-wave basis set. *Comput. Mater. Sci.* **1996**, *6*, 15−50.
(45) Kresse, G.; Furthmüller, J. Efficient iterative schemes for ab initio total-energy calculations using a plane-wave basis set. *Phys. Rev. B* **1996**, *54*, 11169−11186.
(46) Blöchl, P. E. Projector augmented-wave method. *Phys. Rev. B* **1994**, *50*, 17953−17979.
(47) Rostgaard, C. The Projector Augmented-Wave Method. *Phys. Rev. B* **2009**, *62*, 11556−11570.
(48) Cui, P.; Zhao, L.; Long, Y.; Dai, L.; Hu, C. Carbon-Based Electrocatalysts for Acidic Oxygen Reduction Reaction. *Angew. Chem., Int. Ed.* **2023**, *62*, No. e202218269.
(49) Kim, J. H.; Shin, D.; Kim, J.; Lim, J. S.; Paidi, V. K.; Shin, T. J.; Jeong, H. Y.; Lee, K. S.; Kim, H.; Joo, S. H. Reversible Ligand Exchange in Atomically Dispersed Catalysts for Modulating the Activity and Selectivity of the Oxygen Reduction Reaction. *Angew. Chem., Int. Ed.* **2021**, *60*, 20528−20534.
(50) Liu, F.; Shi, L.; Song, S.; Ge, K.; Zhang, X.; Guo, Y.; Liu, D. Simultaneously Engineering the Coordination Environment and Pore Architecture of Metal-Organic Framework-Derived Single-Atomic Iron Catalysts for Ultraefficient Oxygen Reduction. *Small* **2021**, *17*, No. 2102425.
(51) Dudarev, S. L.; Botton, G. A.; Savrasov, S. Y.; Humphreys, C. J.; Sutton, A. P. Electron-energy-loss spectra and the structural stability of nickel oxide: An LSDA1U study. *Phys. Rev. B* **1998**, *57*, 1505−1509.
(52) Mathew, K.; Kolluru, V. S. C.; Mula, S.; Steinmann, S. N.; Hennig, R. G. Implicit self-consistent electrolyte model in plane-wave density-functional theory. *J. Chem. Phys.* **2019**, *151*, No. 234101.
(53) Mathew, K.; Sundararaman, R.; Letchworth-Weaver, K.; Arias, T. A.; Hennig, R. G. Implicit solvation model for density-functional study of nanocrystal surfaces and reaction pathways. *J. Chem. Phys.* **2014**, *140*, No. 084106.
(54) Hu, X.; Chen, S.; Chen, L.; Tian, Y.; Yao, S.; Lu, Z.; Zhang, X.; Zhou, Z. What is the Real Origin of the Activity of Fe-N-C Electrocatalysts in the O(2) Reduction Reaction? Critical Roles of Coordinating Pyrrolic N and Axially Adsorbing Species. *J. Am. Chem. Soc.* **2022**, *144*, 18144−18152.
(55) Rebarchik, M.; Bhandari, S.; Kropp, T.; Mavrikakis, M. How Noninnocent Spectator Species Improve the Oxygen Reduction Activity of Single-Atom Catalysts: Microkinetic Models from First-Principles Calculations. *ACS Catal.* **2020**, *10*, 9129−9135.
(56) Henkelman, G.; Uberuaga, B. P.; Jónsson, H. A climbing image nudged elastic band method for finding saddle points and minimum energy paths. *J. Chem. Phys.* **2000**, *113*, 9901−9904.
(57) Chan, K.; Norskov, J. K. Electrochemical Barriers Made Simple. *J. Phys. Chem. Lett.* **2015**, *6*, 2663−2668.
(58) Chan, K.; Norskov, J. K. Potential Dependence of Electrochemical Barriers from ab Initio Calculations. *J. Phys. Chem. Lett.* **2016**, *7*, 1686−1690.
(59) Nørskov, J. K.; Rossmeisl, J.; Logadottir, A.; Lindqvist, L. Origin of the Overpotential for Oxygen Reduction at a Fuel-Cell Cathode. *J. Phys. Chem. B* **2004**, *108*, 17886−17892.
(60) Wang, F.; Xie, W.; Yang, L.; Xie, D.; Lin, S. Revealing the importance of kinetics in N-coordinated dual-metal sites catalyzed oxygen reduction reaction. *J. Catal.* **2021**, *396*, 215−223.
(61) Leng, K.; Zhang, J.; Wang, Y.; Li, D.; Bai, L.; Shi, J.; Li, X.; Zheng, L.; Bai, J.; Qu, Y. Interfacial Cladding Engineering Suppresses Atomic Thermal Migration to Fabricate Well-Defined Dual-Atom Electrocatalysts. *Adv. Funct. Mater.* **2022**, *32*, No. 2205637.
(62) Zhang, N.; Zhou, T.; Ge, J.; Lin, Y.; Du, Z.; Zhong, C.; Wang, W.; Jiao, Q.; Yuan, R.; Tian, Y.; Chu, W.; Wu, C.; Xie, Y. High-Density Planar-like Fe2N6 Structure Catalyzes Efficient Oxygen Reduction. *Matter* **2020**, *3*, 509−521.
(63) Yang, X.; Shang, C.; Zhou, S.; Zhao, J. MBenes: emerging 2D materials as efficient electrocatalysts for the nitrogen reduction reaction. *Nanoscale Horiz.* **2020**, *5*, 1106−1115.
(64) Wang, J.; Zhang, Z.; Qi, S.; Fan, Y.; Yang, Y.; Li, W.; Zhao, M. Photo-assisted high performance single atom electrocatalysis of the N2 reduction reaction by a Mo-embedded covalent organic framework. *J. Mater. Chem. A* **2021**, *9*, 19949−19957.
(65) Li, L.; Yuan, K.; Chen, Y. Breaking the Scaling Relationship Limit: From Single-Atom to DualAtom Catalysts. *Acc. Mater. Res.* **2022**, *3*, 584−596.
(66) Zhou, X.; Gao, J.; Hu, Y.; Jin, Z.; Hu, K.; Reddy, K. M.; Yuan, Q.; Lin, X.; Qiu, H.-J. Theoretically Revealed and Experimentally Demonstrated Synergistic Electronic Interaction of CoFe Dual-Metal Sites on N-doped Carbon for Boosting Both Oxygen Reduction and Evolution Reactions. *Nano Lett.* **2022**, *22*, 3392−3399.
(67) Sarkar, S.; Biswas, A.; Siddharthan, E. E.; Thapa, R.; Dey, R. S. Strategic Modulation of Target-Specific Isolated Fe,Co Single-Atom Active Sites for Oxygen Electrocatalysis Impacting High Power Zn−Air Battery. *ACS Nano* **2022**, *16*, 7890−7903.
(68) Yang, W.; Huang, H.; Ding, X.; Ding, Z.; Wu, C.; Gates, I. D.; Gao, Z. Theoretical study on double-atom catalysts supported with graphene for electroreduction of nitrogen into ammonia. *Electrochim. Acta* **2020**, *335*, No. 135667.
(69) Wang, J.; Huang, Z.; Liu, W.; Chang, C.; Tang, H.; Li, Z.; Chen, W.; Jia, C.; Yao, T.; Wei, S.; Wu, Y.; Li, Y. Design of N-Coordinated Dual-Metal Sites: A Stable and Active Pt-Free Catalyst for Acidic Oxygen Reduction Reaction. *J. Am. Chem. Soc.* **2017**, *139*, 17281−17284.
(70) Liu, X.; Wei, Z.; Liu, J.; Tan, W.; Fang, X.; Fang, D.; Wang, X.; Wang, D.; Tang, J.; Fan, X. Oxidization of Al0.5Ga0.5As(001) surface: The electronic properties. *Appl. Surf. Sci.* **2018**, *436*, 460−466.
(71) Cen, W.; Liu, Y.; Wu, Z.; Wang, H.; Weng, X. A theoretic insight into the catalytic activity promotion of CeO2 surfaces by Mn doping. *Phys. Chem. Chem. Phys.* **2012**, *14*, 5769−5777.
(72) Xiao, M.; Chen, Y.; Zhu, J.; Zhang, H.; Zhao, X.; Gao, L.; Wang, X.; Zhao, J.; Ge, J.; Jiang, Z.; Chen, S.; Liu, C.; Xing, W. Climbing the Apex of the ORR Volcano Plot via Binuclear Site Construction: Electronic and Geometric Engineering. *J. Am. Chem. Soc.* **2019**, *141*, 17763−17770.
(73) Chen, Y.; Ji, S.; Wang, Y.; Dong, J.; Chen, W.; Li, Z.; Shen, R.; Zheng, L.; Zhuang, Z.; Wang, D.; Li, Y. Isolated Single Iron Atoms Anchored on N-Doped Porous Carbon as an Efficient Electrocatalyst for the Oxygen Reduction Reaction. *Angew. Chem., Int. Ed.* **2017**, *56*, 6937−6941.
(74) Xia, Z.; Yin, Y.; Li, J.; Xiao, H. Single-atom catalysis enabled by high-energy metastable structures. *Chem. Sci.* **2023**, *14*, 2631−2639.
(75) Zhou, T.; Shan, H.; Yu, H.; Zhong, C.; Ge, J.; Zhang, N.; Chu, W.; Yan, W.; Xu, Q.; Wu, H.; Wu, C.; Xie, Y. Nanopore Confinement of Electrocatalysts Optimizing Triple Transport for an Ultrahigh-Power-Density Zinc-Air Fuel Cell with Robust Stability. *Adv. Mater.* **2020**, *32*, No. 2003251.
(76) Liu, T.; Wang, Y.; Li, Y. How pH Affects the Oxygen Reduction Reactivity of Fe−N−C Materials. *ACS Catal.* **2023**, *13*, 1717−1725.
(77) Calle-Vallejo, F.; Krabbe, A.; Garcia-Lastra, J. M. How covalence breaks adsorption-energy scaling relations and solvation restores them. *Chem. Sci.* **2017**, *8*, 124−130.
(78) Liu, M.; Chun, H.; Yang, T.-C.; Hong, S. J.; Yang, C.-M.; Han, B.; Lee, L. Y. S. Tuning the Site-to-Site Interaction in Ru−M (M = Co, Fe, Ni) Diatomic Electrocatalysts to Climb up the Volcano Plot of Oxygen Electroreduction. *ACS Nano* **2022**, *16*, 10657−10666.

https://doi.org/10.1021/jacsau.3c00432
JACS Au 2023, 3, 3031−3044

(79) Gao, R.; Wang, J.; Huang, Z.-F.; Zhang, R.; Wang, W.; Pan, L.; Zhang, J.; Zhu, W.; Zhang, X.; Shi, C.; Lim, J.; Zou, J.-J. Pt/Fe2O3 with Pt−Fe pair sites as a catalyst for oxygen reduction with ultralow Pt loading. *Nat. Energy* **2021**, *6*, 614−623.
(80) Campbell, C. T.; Sellers, J. R. Anchored metal nanoparticles: effects of support and size on their energy, sintering resistance and reactivity. *Faraday Discuss.* **2013**, *162*, 9−30.
(81) Lu, Z.; Yang, Z. Interfacial properties of NM/CeO2(111) (NM = noble metal atoms or clusters of Pd, Pt and Rh): a first principles study. *J. Phys.: Condens. Matter* **2010**, *22*, No. 475003.
(82) Xu, H.; Zhu, L.; Nan, Y.; Xie, Y.; Cheng, D. Revisit the Role of Metal Dopants in Enhancing the Selectivity of Ag-Catalyzed Ethylene Epoxidation: Optimizing Oxophilicity of Reaction Site via Cocatalytic Mechanism. *ACS Catal.* **2021**, *11*, 3371−3383.

https://doi.org/10.1021/jacsau.3c00432
JACS Au 2023, 3, 3031−3044